



# The role of dust mineral composition in atmospheric radiation and pollution in North China: new insights from EMIT and two-way coupled modeling

Chao Gao<sup>1</sup>, Xuelei Zhang<sup>1,2</sup>, Hu Yang<sup>1</sup>, Ling Huang<sup>3</sup>, Hongmei Zhao<sup>1</sup>, Shichun Zhang<sup>1</sup>, and Aijun Xiu<sup>1</sup>

<sup>1</sup>State Key Laboratory of Black Soils Conservation and Utilization, Northeast Institute of Geography and Agroecology, Chinese Academy of Sciences, Changchun, 130102, China

<sup>2</sup>School of Geographical Sciences, Liaoning Normal University, Dalian, 116029, China

<sup>3</sup>School of Environmental and Chemical Engineering, Shanghai University, Shanghai 200444, China

**Correspondence:** Xuelei Zhang (zhangxuelei@neigae.ac.cn)

Received: 10 February 2025 – Discussion started: 28 April 2025

Revised: 14 October 2025 – Accepted: 8 March 2026 – Published: 17 March 2026

**Abstract.** Mineral dust is a major atmospheric aerosol influencing Earth's energy balance through aerosol–radiation (ARI) and aerosol–cloud interactions (ACI). While homogeneous dust effects have been studied, the impact of mineralogical composition on regional meteorology and air quality remains underexplored, limiting accurate forecasting of dust storm impacts, especially in dust belt regions. In this study, we used a two-way coupled WRF-CHIMERE model with three mineralogical dust atlases (Nickovic et al., 2012 (N2012); Journet et al., 2014 (J2014); and a new dataset, Li et al., 2024 (L2024), from the Earth Surface Mineral Dust Source Investigation (EMIT)) to evaluate ARI effects during the March 2021 dust storm in North China. Results showed significant spatial variations in radiative forcing due to mineralogical differences. Bulk dust (without considering mineralogy) caused an average shortwave radiative forcing of  $-5.72 \text{ W m}^{-2}$ , while mineral-specific forcings increased this by up to  $+0.10 \text{ W m}^{-2}$ . Integrating EMIT data reduced  $\text{PM}_{10}$  biases by over 15% in high-concentration regions and improved ozone predictions, with localized changes of  $-2.46$  to  $+3.52 \mu\text{g m}^{-3}$ . Hematite's strong absorption and quartz's reflective properties were key in altering radiative and air quality outcomes. Compared to scenarios of bulk dust, the consideration of ARI effects of mineralogical compositions can increase  $\text{PM}_{10}$  concentration by up to  $1189.48 \mu\text{g m}^{-3}$  in dust source regions. Future research perspectives on the utilization of high-resolution EMIT data in two-way coupled meteorology and air quality models for investigating the ACI effects of mineralogical dust on cloud microphysics are proposed.

## 1 Introduction

Mineral dust, a dominant component of global atmospheric aerosols, primarily originates from wind erosion in arid and semi-arid regions (Schepanski, 2018; Shao et al., 2011). It can affect the Earth's energy balance through direct scattering and absorption of solar, i.e. aerosol–radiation interaction (ARI), as well as indirect effects on cloud properties by acting as cloud condensation nuclei and ice nuclei, i.e., aerosol–cloud interaction (ACI) (Choobari et al., 2014; Kok et al., 2023). By altering biogeochemical cycles, atmospheric chemistry and visibility, and air quality, transported mineral

dust can exacerbate economic losses, and health risks (Adebisi et al., 2023; Cwierny et al., 2008; Duniway et al., 2019; Maher et al., 2010; Tong et al., 2023). Accurate forecasting of mineral dust events is crucial to mitigate these adverse impacts.

Numerous studies have demonstrated that the magnitude of dust ARI and ACI effects is significantly influenced by its mineralogical composition. For instance, iron oxides, particularly hematite and goethite, have been identified as key components responsible for dust absorption of solar radiation, as evidenced by both observational and modeling studies (Alfaro et al., 2004; Gómez Maqueo Anaya et al., 2024;

Lafon et al., 2006; Li et al., 2022; Obiso et al., 2024; Scanza et al., 2015; Song et al., 2024). Concurrently, a growing body of research has explored the impact of various dust mineral compositions, including hematite, corundum, kaolinite, mica, montmorillonite, quartz, calcite, illite, amorphous silicon, aluminum silicate, and potassium feldspar, on ice nucleation processes. Among these, potassium feldspar has emerged as a crucial component for dust nucleation activation (Harrison et al., 2016; Kumar et al., 2018). However, a notable gap exists in our understanding of how specific mineral compositions impact meteorology and air quality through ARI and ACI effects. Prior research has predominantly focused on homogeneous dust aerosols, assuming globally uniform composition and optical properties. However, this assumption introduces regional inaccuracies in estimating the impacts of dust aerosols, which remain poorly understood due to uncertainties in dust composition (Ke et al., 2022; Klingmüller et al., 2019; Kok et al., 2017).

Many efforts have been directed to improve simulations of dust mineralogy and its representation in numerical models (Balkanski et al., 2021; Gómez Maqueo Anaya et al., 2024; Gonçalves Ageitos et al., 2023; Li et al., 2021, 2022, 2024; Li and Sokolik, 2018; Menut et al., 2020; Obiso et al., 2024; Scanza et al., 2015; Solomos et al., 2023b, a; Song et al., 2024). Most of the above are offline models, with only two studies conducting two-way feedback simulations with only WRF-Chem (Li and Sokolik, 2018) and WRF-CHIMERE (Menut et al., 2020) being applied. However, both of these studies are derived from artificially generated data and lack effective ground-based validation, as discussed in Claquin et al. (1999), Nickovic et al. (2012) (N2012 hereafter), and Journet et al. (2014) (J2014 hereafter). These validations predominantly focus on agricultural regions rather than the arid and semi-arid areas that are major sources of dust emissions (Green et al., 2020). EMIT instrument provides a new approach to invert and obtain the surface soil mineral composition and further assess the ARI and ACI effects of dust minerals (Connelly et al., 2021). To the best of our knowledge, no prior research has investigated the impact of dust on regional meteorology and air quality while considering its mineral speciation using two-way coupled models with three different mineralogical dust atlases.

Since the aerosol nucleation processes (ACI effects) of specific mineral components are not represented in the current two-way coupled WRF-CHIMERE framework, the present study concentrates on the ARI effects of dust minerals. This focus ensures a clear and robust assessment of how mineralogical composition influences radiative processes, without introducing additional uncertainties arising from incomplete cloud-related parameterizations. In this study, we employ a two-way coupled WRF-CHIMERE model with three mineralogical databases to investigate how dust composition influences radiation and meteorology in North China during a severe dust storm. Section 2 describes the model configuration and data sources, Sect. 3 presents the simula-

tions with emphasis on ARI-induced impacts on meteorology and air quality, and Sect. 4 summarizes the main findings.

## 2 Methodology and data

### 2.1 Model configurations and data sources

The two-way coupled WRF model version 3.7.1 and CHIMERE model version 2020r3 were employed to simulate the ARI and ACI effects of mineralogical dust particles on meteorology and air quality over North China from 12 to 15 March 2021. The exchanges between meteorological and air quality variables are accomplished through the OASIS coupler (Briant et al., 2017). The simulation was conducted at a horizontal resolution of 27 km, with 165 grid cells in the east-west direction and 87 in the north-south direction, and the study domain is depicted in Fig. S1 in the Supplement. The model has 33 vertical levels from surface to 50 hPa with 13 layers in the bottom 1 km and the bottom thickness being 24.5 m. The Rapid Radiative Transfer Model for General circulation models (RRTMG) shortwave and longwave radiation schemes were employed to investigate the ARI effects (Briant et al., 2017). Additionally, the Thompson cloud microphysics scheme was utilized to assess the impacts of ACI (Tuccella et al., 2019). The initial and boundary conditions (ICs and BCs) for non-dust aerosols are prescribed by the LDMZ-INCA model, while those for dust aerosols are determined by the GOCART model. The options of other physics and chemistry schemes are presented in Table S1 in the Supplement. The dry depositions are treated as described in Zhang et al. (2001). The parameterizations for the removal of dust particles below clouds by raindrops and snow are based on the methods proposed by Willis and Tattelman (1989) and Wang et al. (2014), respectively. Inline mineral dust emissions, incorporating mineralogy, are computed using a  $u^*$  threshold and a dust production model for saltation (Kok et al., 2014; Shao and Lu, 2000). The model accounts for the impact of soil moisture on suppressing mineral dust emissions (Fécan et al., 1998). To minimize meteorological bias, a spectral nudging approach is applied (Menut et al., 2024).

For the calculations of ARI effects in WRF-CHIMERE, refractive indices corresponding to these mineralogical species are provided in Table 2 of Menut et al. (2020). Concerning shortwave (SW) radiation, the aerosol optical properties, encompassing single scattering albedos and asymmetry factors at 400 and 600 nm, as well as the aerosol optical depth (AOD) at 300, 400, and 999 nm, calculated using Fast-JX, were interpolated or extrapolated to obtain values at 14 SW intervals (Briant et al., 2017; Gao et al., 2022). AOD at 16 longwave (LW) intervals ranging from 3400 to 55 600 nm are directly used to calculate LW radiation.

To evaluate the performance of the WRF-CHIMERE model with and without mineralogical dust emissions, we compiled a comprehensive set of environmental observa-

**Table 1.** Mineralogical compositions in different datasets.

Mineral	Clay		Silt		EMIT
	N2012	J2014	N2012	J2014	
Smectite	✓	✓	✗	✗	✓
Illite	✓	✓	✗	✗	✓*
Hematite	✓	✓	✓	✗	✓
Feldspar	✗	✓	✓	✓	✗
Kaolinite	✓	✓	✗	✗	✓
Calcite	✓	✓	✓	✓	✓
Quartz	✓	✓	✓	✓	✗
Gypsum	✗	✗	✓	✓	✓
Vermiculite	✗	✓	✗	✗	✓
Chlorite	✗	✓	✗	✓	✓
Goethite	✗	✗	✗	✓	✓
Mica	✗	✗	✗	✓	✓*
Resolution	1 km	0.5°	1 km	0.5°	0.5°

\* Indicates the content of illite + mica.

tions, as shown in Fig. S1. Hourly PM<sub>10</sub> and O<sub>3</sub> concentrations (132 observations) were obtained from <https://quotsoft.net/air/> (last access: 14 March 2026), which aggregates official monitoring data from the Ministry of Ecology and Environmental Protection of China. Shortwave radiation (SSR) data (59 hourly measurements) were obtained from Tang et al. (2019), with the original measurements sourced from the China Meteorological Administration. Hourly surface meteorological data (844 observations) were also obtained from the China Meteorological Administration (<https://data.cma.cn>, last access: 14 March 2026). All datasets were subjected to quality control procedures, including checks for outliers, unit consistency, and temporal alignment, to ensure reliability and integrity.

## 2.2 Mineral dust atlases

Accurate soil composition data are essential for partitioning dust emission fluxes into contributions from individual minerals. Mineral density and refractive index data were obtained from Menut et al. (2020). Three global mineralogical composition datasets (N2012, J2014, and EMIT) provide information on 12 mineral species (Table 1) at different spatial resolutions (1 km × 1 km and 0.5° × 0.5°).

To ensure a consistent spatial framework and facilitate cross-dataset integration, the N2012 dataset (originally provided at 1 km × 1 km resolution and available at <http://www.seevccc.rs/GMINER30>, last access: 14 March 2026) was resampled to 0.5° × 0.5°. The J2014 dataset, widely employed in the WRF–CHIMERE modeling framework, includes 12 mineral species distributed across the clay and/or silt fractions (see Table 2 in Menut et al., 2020). In contrast, the EMIT dataset (<https://earth.jpl.nasa.gov/emit/data/data-products>, last access: 14 March 2026) required addi-

tional preprocessing, as it reports only normalized spectral abundances rather than mineral mass fractions. These spectral abundances were therefore recalculated to represent the normalized mass proportions of each mineral in each substrate. Furthermore, EMIT does not include data for feldspar and quartz, necessitating additional correction procedures described below.

When the total mineral composition from EMIT summed to less than 100 %, indicating missing mineral contributions, the residual fraction was assigned to quartz and feldspar based on their relative proportions in J2014 or N2012. Because EMIT reports illite and mica as a single category, their individual abundances were separated according to the ratios found in N2012 or J2014. For minerals that occur in both clay and silt fractions, EMIT values were partitioned following the relative contributions from N2012 or J2014.

For minerals not directly observed by EMIT (e.g., quartz and feldspar), their mass fractions were estimated using soil-type conversion methods from previous studies (Claquin et al., 1999; Journet et al., 2014). The spatial distributions of clay and silt were obtained from the global SoilW texture dataset (<http://globalchange.bnu.edu.cn/research/soilw>, last access: 14 March 2026) at 1 km resolution and resampled to 0.5° to match EMIT data. Similarly, the J2014 and N2012 mineral datasets were resampled to 0.5° resolution. Major minerals extracted from EMIT L3 include calcite, dolomite, chlorite, goethite, gypsum, hematite, illite + mica, kaolinite, montmorillonite, and vermiculite. Notably, in the official EMIT L3B dataset ([https://data.lpdaac.earthdatacloud.nasa.gov/lp-prod-protected/EMITL3ASA.001/EMIT\\_L3\\_ASA\\_001/EMIT\\_L3\\_ASA\\_001.nc](https://data.lpdaac.earthdatacloud.nasa.gov/lp-prod-protected/EMITL3ASA.001/EMIT_L3_ASA_001/EMIT_L3_ASA_001.nc), last access: 14 March 2026), illite and mica are combined because they were jointly identified during the Tetracorder analysis of L2B data using mineral groups 1 and 2 and the corresponding band depths ([https://github.com/nasa/EMIT-Data-Resources/blob/main/data/mineral\\_grouping\\_matrix\\_20230503.csv](https://github.com/nasa/EMIT-Data-Resources/blob/main/data/mineral_grouping_matrix_20230503.csv), last access: 14 March 2026).

The EMIT mineral fractions were normalized so that their sum at each grid point did not exceed unity. Any remaining fraction was attributed to quartz and feldspars according to their relative proportions in J2014 or N2012. To ensure consistency with the CHIMERE mineral representation, dolomite was merged into calcite, illite + mica was separated into illite and mica, and montmorillonite was treated as smectite. The mineral fractions were then converted to density-weighted values and renormalized at each grid point so that the total sum equaled one. Finally, each mineral was partitioned into clay and silt fractions based on the J2014 ratios, and the resulting fractions were normalized using Eqs. (1)–(4). The processed dataset was exported as a NetCDF file to serve as input for the CHIMERE model.

To ensure mineral mass balance and model consistency, a normalization and partitioning procedure was applied as follows. Equation (1) defines the total mass fraction (MF<sub>*j*</sub>) of mineral *j* as the sum of its contributions from the clay

(MFC<sub>*j*</sub>) and silt (MFS<sub>*j*</sub>) fractions:

$$MF_j = MFC_j + MFS_j \text{ for all } j \in M_{\text{CHIMERE}} \quad (1)$$

Equation (2) enforces a normalization constraint so that the sum of all mineral mass fractions equals unity at each grid point.

$$1 = \sum_{j \in M_{\text{CHIMERE}}} MF_j \quad (2)$$

The normalized total fraction of each mineral (MF<sub>*j*</sub><sup>\*</sup>) was then redistributed between clay and silt according to their relative contributions in the reference dataset (J2014 or N2012), as shown in Eqs. (3) and (4):

$$MFS_j^* = MF_j^* \frac{MFS_j}{MFS_j + MFC_j} \quad (3)$$

$$MFC_j^* = MF_j^* \frac{MFC_j}{MFS_j + MFC_j} \quad (4)$$

here, MFS<sub>*j*</sub><sup>\*</sup> and MFC<sub>*j*</sub><sup>\*</sup> represent the normalized mass fractions of mineral *j* in the silt and clay fractions, respectively. The weighting terms MFS<sub>*j*</sub> and MFC<sub>*j*</sub> preserve the clay–silt distribution patterns derived from the reference datasets while maintaining the normalized total (MF<sub>*j*</sub><sup>\*</sup>).

### 2.3 Scenario set up

Ten parallel WRF-CHIMERE simulations were performed to investigate the influence of mineralogical dust on meteorology and air quality in China, employing three distinct mineralogical atlases, as illustrated in Figs. 1 and S5–S7. Each simulation was conducted both with and without enabling ARI effects, as detailed in Table 2, to isolate and compare the effects of mineralogical dust under different modeling conditions.

Simulations without ARI effects (Dust\_NO, N2012\_Default\_NO, N2012\_EMIT\_NO, J2014\_Default\_NO, J2014\_EMIT\_NO) were specifically designed to identify the direct impact of mineralogical dust on meteorology and air quality, independent of the radiative feedbacks induced by aerosols. These No\_ARI simulations served as a baseline for assessing how mineralogical compositions affect meteorology and air quality in the absence of aerosol–radiation feedback mechanisms.

In contrast, simulations with ARI enabled (Dust\_ARI, N2012\_Default\_ARI, N2012\_EMIT\_ARI, J2014\_Default\_ARI, J2014\_EMIT\_ARI) were used to quantify the additional effects arising from aerosol–radiation interactions. By comparing simulations with and without ARI for each mineralogical atlas (e.g., N2012\_Default\_ARI – N2012\_Default\_NO), the differential impact of ARI effects on meteorology and air quality for various dust compositions could be identified. This approach highlights how mineralogical properties of dust influence the strength and nature of ARI effects, thereby modulating key atmospheric

processes such as radiation balance, temperature profiles, and pollutant distributions.

To evaluate the discrepancies in ARI effects among the mineralogical atlases, differences in the ARI impacts between EMIT-derived and default dust compositions were analyzed for both N2012 and J2014 datasets. For example, comparisons such as (N2012\_EMIT\_ARI – N2012\_EMIT\_NO) versus (N2012\_Default\_ARI – N2012\_Default\_NO) provide insight into the extent to which higher-resolution, satellite-derived mineralogical data influence ARI effects relative to default atlas-based representations. Similar comparisons were performed for the J2014 dataset.

## 3 Results and discussion

### 3.1 Evaluation of meteorology and air quality

Table 3 presents the evaluation results for observed and simulated surface shortwave radiation (SSR), 2 m temperature (T2), and 10 m wind speed (WS10) from various scenario simulations conducted using the WRF-CHIMERE modeling system. The model demonstrates strong overall performance, with correlation coefficients (*R*) between observed and simulated values reaching approximately 0.7 for SSR and WS10, and up to 0.93 for T2. These results indicate the model's ability to capture key atmospheric patterns and variability across the simulation domain. Nevertheless, systematic biases are apparent, particularly in North China, where the model tends to overestimate SSR and WS10 by 60.69%–68.92% and 17.06%–17.52%, respectively, while underestimating T2 by 0.48%–0.58%. The overestimation of SSR likely results from uncertainties in cloud development associated with planetary boundary layer and convection parameterizations (Alapaty et al., 2012). The systematic overestimation of 10 m wind speed under low-wind conditions commonly observed in weather models mainly stems from outdated geographic data and coarse spatial resolution (Gao et al., 2024).

A comparative analysis of the two configurations, N2012 and J2014, reveals that WRF-CHIMERE with N2012 generally outperforms J2014 in simulating SSR and T2, suggesting that the N2012 parameterization better captures radiative and thermodynamic processes in the region. Conversely, J2014 exhibits improved accuracy in simulating WS10, implying potential strengths in its representation of near-surface wind dynamics. These findings highlight the sensitivity of model performance to parameterization schemes and the need for tailored configurations for specific meteorological variables. The inclusion of detailed dust mineralogical compositions, while informative for certain applications, introduces additional complexities that reduce the overall accuracy of simulations. Specifically, while these compositions help mitigate the overestimation of SSR and the underestimation of T2, they exacerbate the overestimation of WS10. The integration

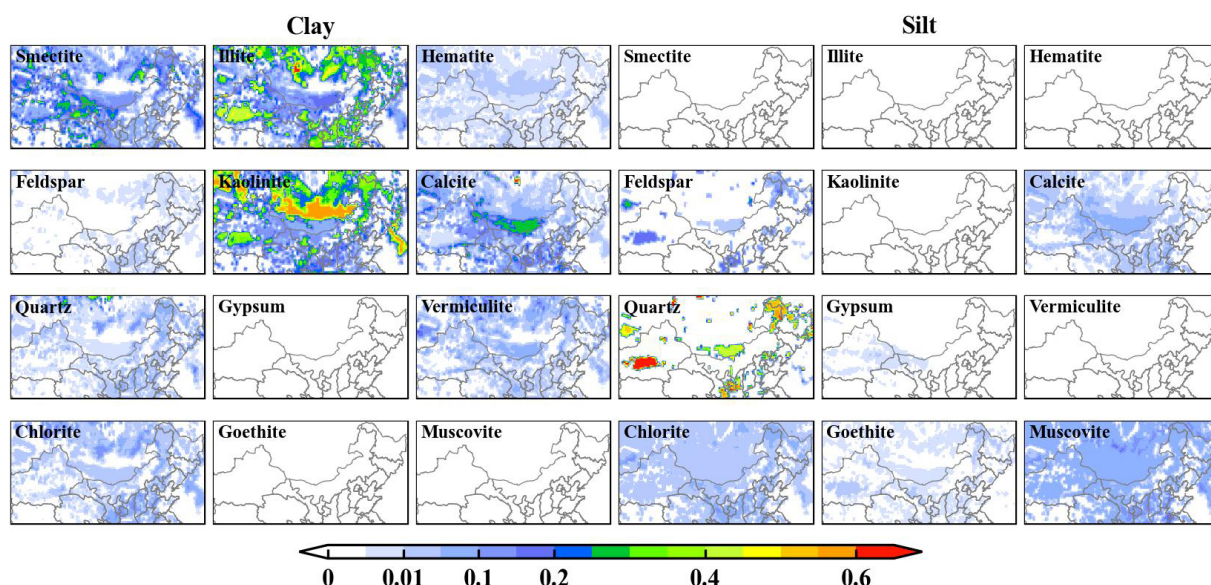


**Figure 1.** Spatial distribution of content for the different mineral dust species in the silt and clay fraction of the soil for original J2014 mineralogical data.

**Table 2.** Summary of dust emission scenarios and aerosol feedback configurations for different simulation settings.

Scenario	Emission	Online choice	Coupling type	Aerosol feedback
Dust_NO	Bulk dust + anthropogenic emissions	[online] = 1	[cpl_case] = 1	No feedbacks
Dust_ARI		[online] = 1	[cpl_case] = 2	ARI effects
N2012_Default_NO	N2012_Default dust + anthropogenic emissions	[online] = 1	[cpl_case] = 1	No feedbacks
N2012_Default_ARI		[online] = 1	[cpl_case] = 2	ARI effects
N2012_EMIT_NO	N2012_EMIT dust + anthropogenic emissions	[online] = 1	[cpl_case] = 1	No feedbacks
N2012_EMIT_ARI		[online] = 1	[cpl_case] = 2	ARI effects
J2014_Default_NO	J2014_Default dust + anthropogenic emissions	[online] = 1	[cpl_case] = 1	No feedbacks
J2014_Default_ARI		[online] = 1	[cpl_case] = 2	ARI effects
J2014_EMIT_NO	J2014_EMIT dust + anthropogenic emissions	[online] = 1	[cpl_case] = 1	No feedbacks
J2014_EMIT_ARI		[online] = 1	[cpl_case] = 2	ARI effects

of EMIT satellite data provides a significant boost to model performance, highlighting the value of incorporating high-resolution, real-time observational data to refine the simulation of atmospheric variables. EMIT data, with its detailed characterization of aerosol and dust properties, reduces the positive biases in SSR and WS10 while simultaneously minimizing the negative biases in T2.

When comparing the ARI effects of the defaulted mineralogical compositions in N2012 and J2014 with simulations that implement EMIT satellite data, the latter shows a clear advantage. Incorporating EMIT data further reduces the positive biases in SSR and WS10, while simultaneously minimizing the negative biases in T2. This suggests that EMIT data provides a more precise representation of dust properties and atmospheric conditions, enhancing the overall reliability of the model.

To assess the ability of each scenario simulation to replicate regional PM<sub>10</sub> and O<sub>3</sub> temporal patterns, Fig. 2 presents hourly time series of simulated and in situ PM<sub>10</sub> and O<sub>3</sub> concentrations at four North China sites: Ordos, Kalgan, Beijing, and Tianjin. These locations represent key dust aerosol transport pathways, which play a crucial role in the region's air quality dynamics due to frequent dust storms and anthropogenic emissions. The time series plots regarding PM<sub>10</sub> and O<sub>3</sub> in Figs. 2 and S2 allow for a direct comparison of model simulations with observed data, revealing important insights into model performance across different environmental conditions and geographical settings, respectively. The models exhibit relatively high correlations for PM<sub>10</sub>, with *R* values ranging from 0.61 to 0.89 and NMBs from −73.8 % to −0.9 %. In contrast, their performance for O<sub>3</sub> is notably weaker, with *R* values between 0.25 and 0.63 and

**Table 3.** Statistics analysis of daily averaged SSR, 2 m temperature (T2) and 10 m wind speed (WS10) from different scenario simulations and ground observations in North China including correlation coefficient (*R*) and normalized mean bias (NMB).

Scenario	SSR		T2		WS10	
	<i>R</i>	NMB (%)	<i>R</i>	NMB (%)	<i>R</i>	NMB (%)
Dust_NO	0.70	68.92	0.93	−0.58	0.71	17.06
Dust_ARI	0.72	60.69	0.94	−0.48	0.72	17.46
N2012_Default_NO	0.70	68.92	0.93	−0.58	0.71	17.06
N2012_Default_ARI	0.71	61.80	0.94	−0.48	0.72	17.53
N2012_EMIT_NO	0.70	68.92	0.93	−0.58	0.71	17.06
N2012_EMIT_ARI	0.72	60.88	0.94	−0.48	0.72	17.44
J2014_Default_NO	0.70	68.92	0.93	−0.58	0.71	17.06
J2014_Default_ARI	0.71	61.68	0.94	−0.48	0.72	17.51
J2014_EMIT_NO	0.70	68.92	0.93	−0.58	0.71	17.06
J2014_EMIT_ARI	0.72	61.22	0.94	−0.48	0.72	17.48

NMBs from +10.9% to +84.2%. Among the simulations, N2012 with EMIT data and ARI effects provides the best performance for PM<sub>10</sub>, while N2012 with EMIT data without aerosol effects performs best for O<sub>3</sub> concentrations. All models accurately captured the peak PM<sub>10</sub> and O<sub>3</sub> concentrations observed during the 12 March event in North China, which was characterized by significant dust emissions and high pollutant levels. This event serves as a key test case for evaluating the models' responsiveness to extreme atmospheric conditions. However, despite the overall agreement in peak concentration timings, simulations overestimated O<sub>3</sub> and underestimated PM<sub>10</sub> at sites with high dust loads, such as Ordos and Kalgan. This discrepancy highlights the challenge of simulating the complex interactions between dust aerosols, precursor gases, and photochemical reactions, particularly in regions with high dust deposition and frequent air pollution episodes. Additionally, the models tended to extend the period of elevated PM<sub>10</sub> concentrations beyond the observed time frame, suggesting that the processes controlling dust aerosol removal or dispersion were not fully captured. CHIMERE simulations using J2014 mineralogical data generally outperformed those using J2012 data, with significant reductions in PM<sub>10</sub> negative NMBs for three of the four cities, indicating the importance of accurate mineralogical characterization of dust for improving model predictions. When considering the ARI effects of bulk dust aerosols, the underestimation of PM<sub>10</sub> was alleviated, whereas the overestimation of O<sub>3</sub> was amplified, which suggests that incorporating ARI effects helps to better represent the impact of dust on local radiative forcing and air quality. Moreover, incorporating ARI effects from the default dust mineralogical atlas further enhanced these trends, underscoring the need for refined aerosol property data in enhancing model performance. Finally, using Earth-observing systems such as the EMIT satellite data led to substantial reductions in PM<sub>10</sub> negative bias at Kalgan, Beijing, and Tianjin, demonstrating the value of remote sensing data in improving model accuracy, partic-

ularly for regions with high aerosol concentrations and complex emission sources. Although considerable progress has been made in dust modeling, notable uncertainties remain. The parameterization of threshold friction velocity and soil texture in emission schemes can still result in underestimated emissions under strong winds (Zuo et al., 2024). Similarly, simplifications in coarse particle size distributions may lead to enhanced deposition and transport losses. In addition, incomplete knowledge of local soil mineralogical composition continues to limit the accurate simulation of both emission fluxes and heterogeneous chemistry (Pang et al., 2024).

To evaluate the model performance in simulating the horizontal distribution and vertical profile of dust aerosol, Fig. 3 presents the false RGB imagery of dust derived from Himawari-8 thermal infrared imagery, along with CALIPSO cross sections of 532 nm total attenuated backscatter and the vertical feature mask for the overpass of China. The figure also includes the corresponding spatial distributions of PM<sub>10</sub> concentrations at 05:00 UTC on 15 March 2021, a time of significant dust transport in the region. This detailed comparison allows for a comprehensive assessment of how well the model captures both the horizontal and vertical characteristics of dust aerosol distribution. All six experiments display similar dust distributions in the atmosphere, consistent with observations from Himawari-8 and CALIPSO. This suggests that the models effectively capture the general spatial patterns of dust transport. On 15 March 2021, the daily domain-averaged PM<sub>10</sub> concentration was 533.81 μg m<sup>−3</sup>, with a 95% confidence interval (CI) of 0.28–5962.95 (Table S2). Specifically, the false RGB imagery from Himawari-8 clearly indicates the presence of dust plumes in the atmosphere, with distinct thermal contrasts that help identify the dust layers. The CALIPSO data, which provide vertical profiles of aerosol backscatter, further validate the model's ability to capture the vertical extent and concentration of dust layers. These observations are critical for understanding the atmospheric processes governing dust dispersion and their

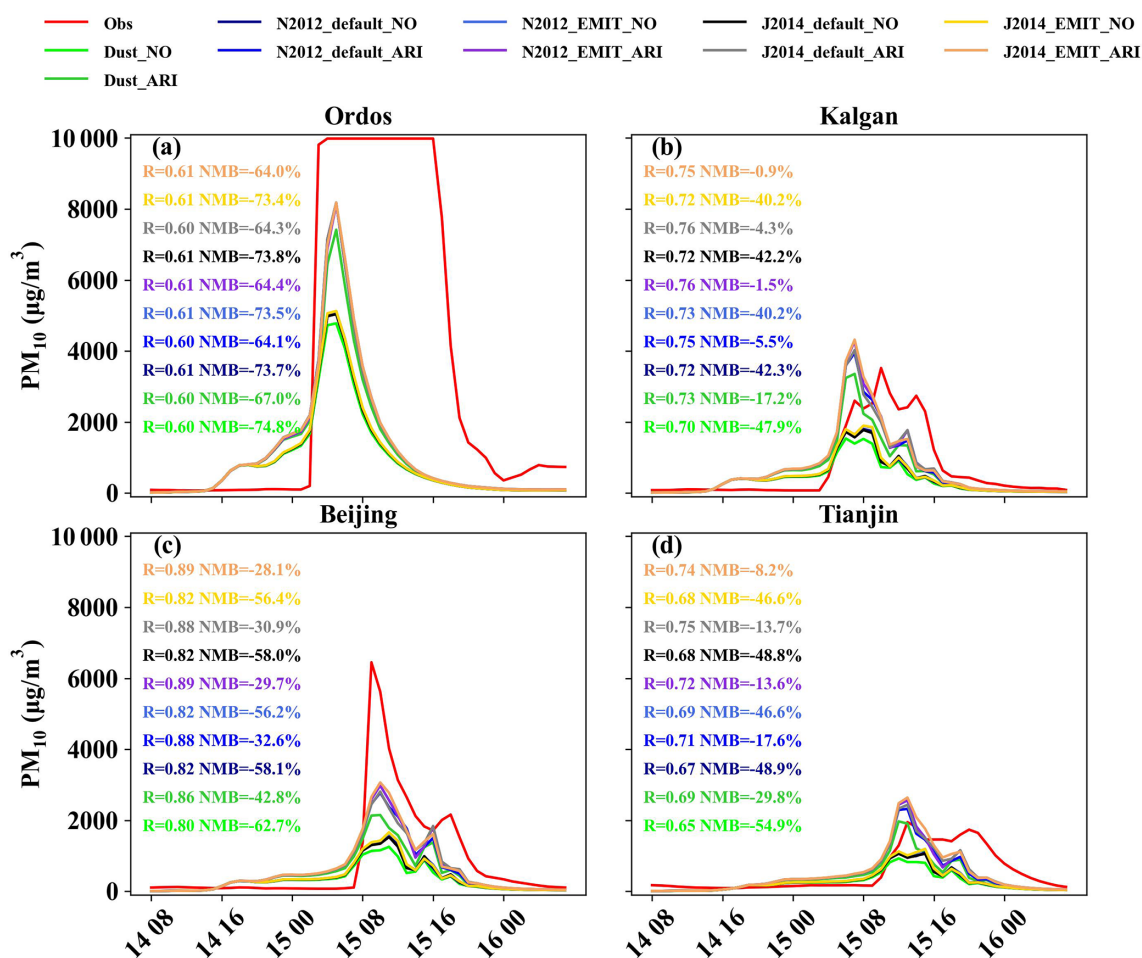


**Figure 2.** Statistical metrics between observed and simulated PM<sub>10</sub> concentrations by different scenario simulations.

impact on air quality. The close agreement between model simulations and satellite data across all six experiments also underscores the robustness of the model in representing dust aerosol distribution under different simulation conditions. This evaluation demonstrates that the models are capable of simulating the main features of dust aerosol transport, though further refinement in capturing the fine-scale variations and aerosol properties may still be necessary for more accurate predictions in future studies.

### 3.2 Radiative effect on meteorology

To further investigate the impacts of dust radiation on energy balance, the spatial distributions of the average short-wave (SW), longwave (LW), and net (NET) radiative forcing induced by bulk dust on the surface (SFC), in the atmosphere (ATM), and at the top of the atmosphere (TOA) are presented during the dust episode shown in Fig. 4. The radiative forcing values provide critical insights into the energy exchanges between dust aerosols and the atmosphere, and their subsequent effects on regional climate dynamics.

For SW radiation forcings, dust aerosols produced cooling effects at all three layers: the surface, the atmosphere, and the top of the atmosphere. The average SW radiative forcing was about  $-5.72 \text{ W m}^{-2}$  at the surface,  $-8.69 \text{ W m}^{-2}$  in the atmosphere, and  $-2.97 \text{ W m}^{-2}$  at the TOA, highlighting the significant reduction in solar radiation reaching these layers due to the scattering and absorption properties of the dust particles. Particularly in the dust source regions, the cooling effect at the surface exceeded  $-900 \text{ W m}^{-2}$  (Fig. 4a, d, and g), indicating the strong influence of dust on the regional energy budget in these areas. This is a result of the large dust concentrations and their optical properties, which effectively block solar radiation from reaching the Earth's surface. In contrast, the dust-induced LW radiative forcing warmed the surface and atmosphere, with average values ranging from  $5.78$  to  $5.86 \text{ W m}^{-2}$ . This warming effect is associated with the absorption of longwave radiation by dust particles, which then re-radiate heat, contributing to local warming. However, dust particles induced negative LW radiative forcing at the TOA, with values ranging from  $-461.88$  to  $-379.95 \text{ W m}^{-2}$ , reflecting the downward flux of longwave radiation absorbed

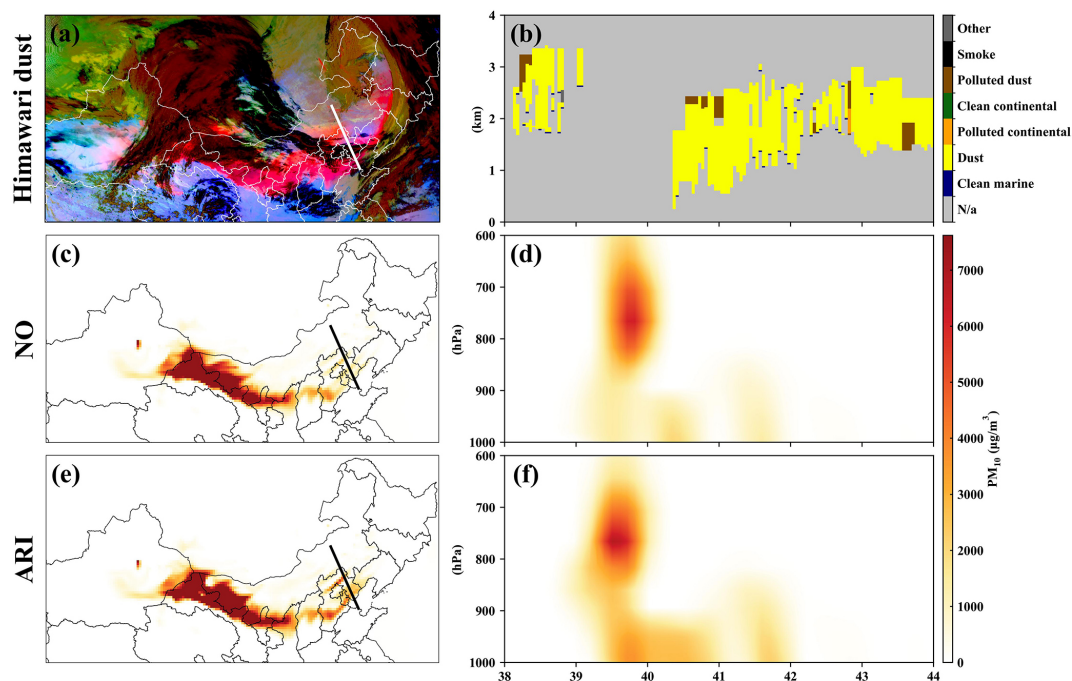


**Figure 3.** The false color imagery of dust from Himawari-8 thermal infrared imagery (a), CALIPSO cross sections of 532 nm total attenuated backscatter and the vertical feature mask for the overpass of China on 13:00 LT, 15 March 2021 (b), and corresponding horizontal (c, e) and vertical (d, f) distributions of  $PM_{10}$  concentrations.

by the aerosols, which reduces the amount of energy reaching the TOA. The NET radiative forcing, which represents the combined effect of both SW and LW forcings, was positive at the surface (about  $+0.15 \text{ W m}^{-2}$ ), negative in the atmosphere (about  $-2.91 \text{ W m}^{-2}$ ), and negative at the TOA (about  $-3.06 \text{ W m}^{-2}$ ), as shown in Fig. 4c, f, and i. The positive NET radiative forcing at the surface suggests a slight net warming effect at ground level, while the negative values in the atmosphere and at the TOA indicate an overall cooling effect at these higher altitudes.

To assess the impact of dust mineralogical composition on radiative forcings, Fig. 5 illustrates the spatial distribution of radiative differences, considering the ARI effects of bulk dust and comparing them to the default N2012 mineralogy atlas. This comparison provides valuable insights into how variations in the mineralogical composition of dust particles can influence the energy balance in the atmosphere. Compared to the ARI effects of bulk dust, the mineralogical composition of dust aerosols can lead to increases in SW radiation forcings at the surface and in the atmosphere, ranging from  $+0.10$  to  $+0.82 \text{ W m}^{-2}$ . This increase reflects the different optical properties of dust mineral types, which can affect the scattering and absorption of solar radiation. These variations in the SW radiation forcings are particularly important for understanding how different dust types modulate the amount of solar radiation reaching the Earth's surface and atmosphere. At the TOA, however, the mineralogical composition resulted in a decrease of about  $-0.72 \text{ W m}^{-2}$  in SW

radiation forcing, suggesting that certain mineralogical types may be more efficient at reflecting solar radiation back into space. Similar to SW radiation forcings, net radiation forcings at the surface and in the atmosphere increased, ranging from  $+0.02$  to  $+0.63 \text{ W m}^{-2}$ , while at the TOA, net radiation forcings decreased by about  $-0.65 \text{ W m}^{-2}$ . The increase in net radiation at the surface and in the atmosphere reflects the combined effect of increased SW absorption and the potential changes in longwave (LW) radiative properties. For LW radiation forcings, the mineralogical composition of dust led to decreases in the radiative forcing across different layers, ranging from  $-0.72$  to  $-0.12 \text{ W m}^{-2}$ . This decrease suggests that certain dust mineral types are more efficient at absorbing and emitting longwave radiation, which can contribute to cooling effects in the atmosphere and at the surface.

As demonstrated in Fig. S3, the selection of the soil mineralogy dataset and the modeling approach significantly influences the calculated dust radiative forcings. When comparing shortwave dust radiative effects (DRE) from WRF-CHIMERE simulations using the default N2012 and J2014 mineral atlases, we observe a minor discrepancy in the DRE amplitude, particularly for shortwave and net radiation forcing at the surface. This discrepancy suggests that the choice of mineralogical dataset can influence the magnitude of radiative forcings, especially under varying atmospheric conditions. Previous research has highlighted the distinct optical properties of hematite and goethite in the shortwave spectrum (Lafon et al., 2006; Sokolik and Toon, 1999). These dif-

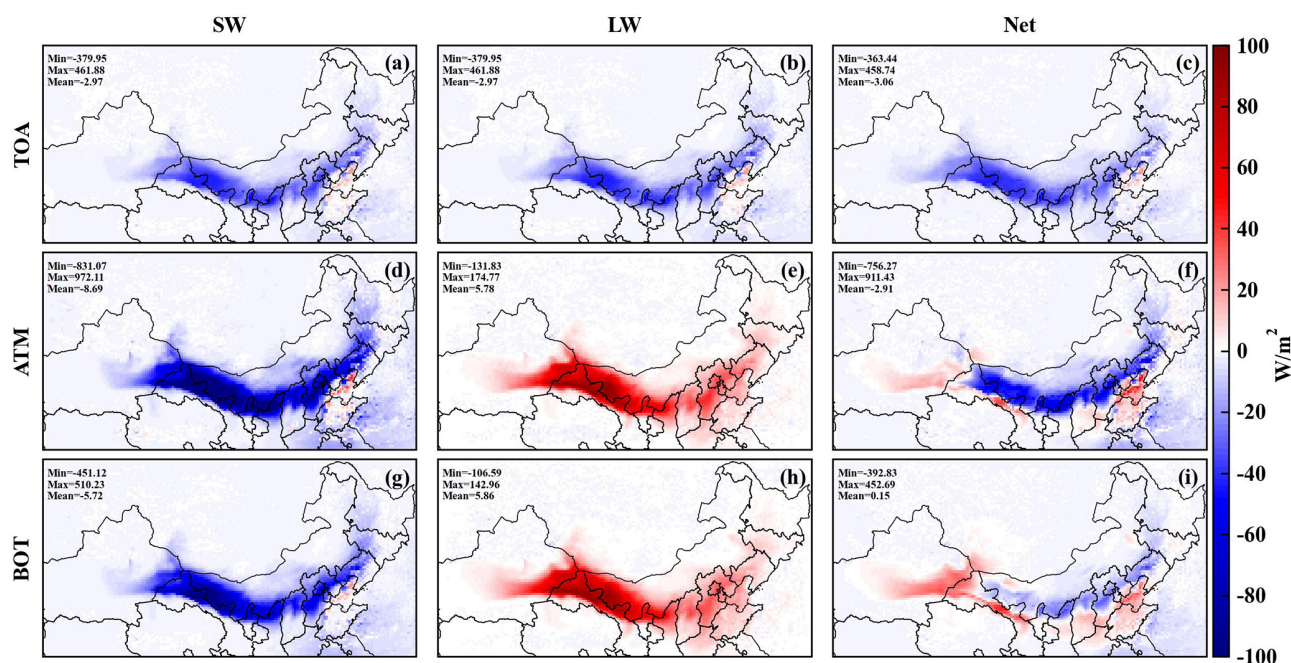


**Figure 4.** Radiation forcings due to bulk dust enabling ARI effects.

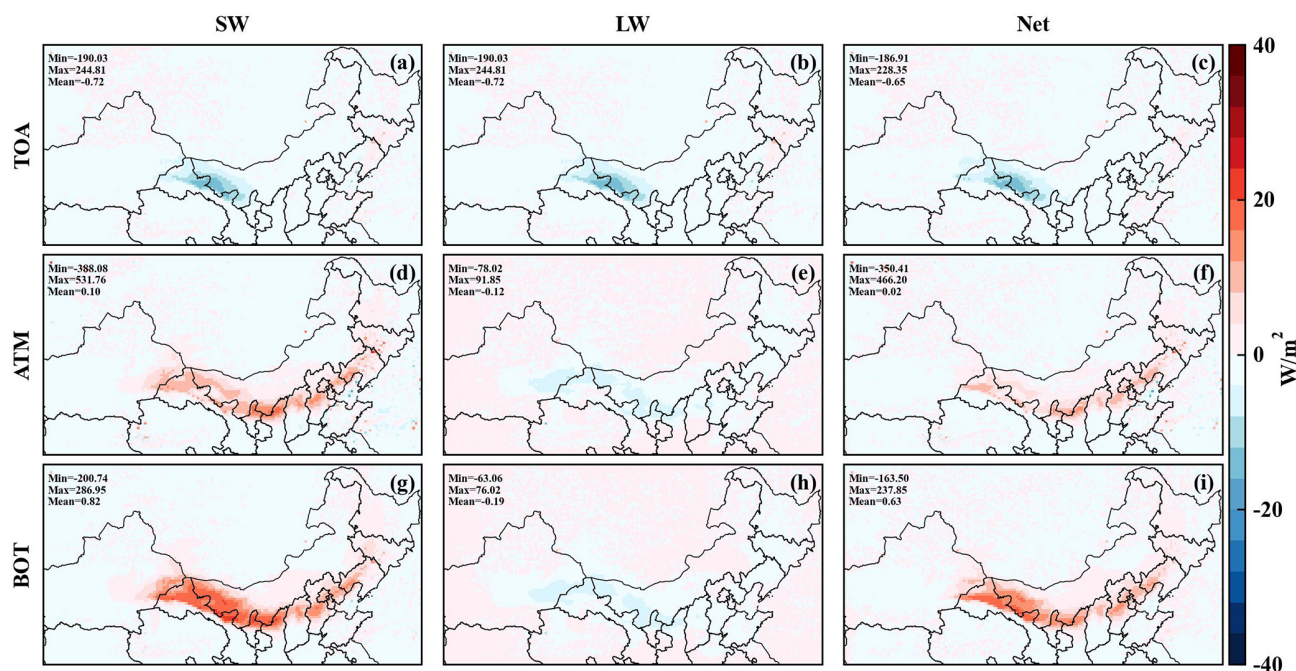


**Figure 5.** Difference between TOA, ATM and BOT radiation forcings with considering bulk dust and mineralogical dust compositions (i.e., N2012\_Default) enabling ARI effects.

ferences contribute to variations in the dust's radiative properties and, in turn, its effect on energy transfer in the atmosphere. Incorporating both minerals in dust production results in a flatter spectral single scattering albedo (SSA), as goethite's less pronounced dependence on shortwave wavelengths reduces the overall absorption in the shortwave spec-

trum (Formenti et al., 2014). This effect is particularly noticeable when comparing the radiative forcings from the different mineralogy datasets, as the presence of goethite alters the absorption and scattering characteristics of the dust particles.

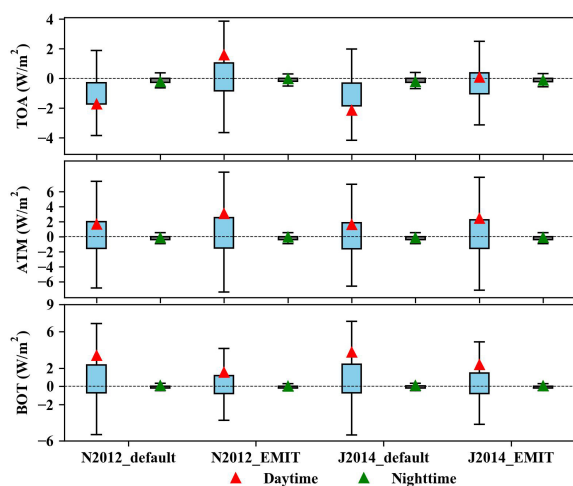


**Figure 6.** Day-night changes of TOA, ATM and BOT shortwave radiation forcings from simulations using different composition atlases (N2012\_Default, N2012\_EMIT, J2014\_Default and J2014\_EMIT) compared to bulk dust.

As depicted in Fig. 6, the distinct day-night variations in shortwave radiation forcing (SWRF) induced by ARI effects have been thoroughly demonstrated when considering different mineralogical atlases compared to bulk dust. These variations reflect the different impacts that dust aerosols have on solar radiation during the day and night, with a clear difference in the magnitude of the effects between the two periods. Notably, SWRF variations were more pronounced during the daytime than at night, which can be attributed to the stronger interaction between dust aerosols and incoming solar radiation during daylight hours. The presence of dust aerosols alters the reflection, absorption, and scattering of sunlight, leading to significant changes in the radiation balance, especially during the day when solar energy is at its peak.

Incorporating default dust mineralogical compositions into the simulations led to an increase in daytime SWRF at the surface and within the atmosphere, ranging from 1.60 to 3.74  $\text{W m}^{-2}$ . This increase suggests that the specific mineralogy of dust aerosols contributes to greater absorption and scattering of solar radiation, amplifying the cooling effect at the surface and the atmosphere. However, at the top of the atmosphere (TOA), the SWRF decreased by approximately 2.00  $\text{W m}^{-2}$ , which could be indicative of increased reflection of shortwave radiation back into space due to the dust particles' optical properties. This shift in radiative forcing at the TOA highlights the role of dust in altering the energy fluxes across different atmospheric layers.

When comparing simulations using default dust mineralogical compositions to those employing Earth-observing EMIT satellite data within the WRF-CHIMERE model, notable differences in SWRF were observed. Daytime SWRF at the surface was reduced for the N2012 mineralogy dataset ( $-1.88 \text{ W m}^{-2}$ ) and J2014 mineralogy dataset

( $-1.37 \text{ W m}^{-2}$ ) when using EMIT data, compared to the default dust mineralogy compositions. This reduction could be due to more accurate mineralogical characterization, which alters the dust's optical properties and reduces its ability to absorb and scatter sunlight. Conversely, SWRF was enhanced in the atmosphere (N2012:  $+1.44 \text{ W m}^{-2}$ , J2014:  $+0.84 \text{ W m}^{-2}$ ) when using the EMIT data, indicating that the updated mineralogical information leads to a different interaction with solar radiation in the atmospheric layer, possibly due to changes in dust composition that affect scattering and absorption properties at higher altitudes.

Furthermore, SWRF at the TOA transitioned from negative to positive in simulations using the EMIT data. For the N2012 dataset, the SWRF varied from  $-1.73$  to  $+1.59 \text{ W m}^{-2}$ , and for the J2014 dataset, it ranged from  $-2.14$  to  $+0.07 \text{ W m}^{-2}$ . This shift suggests that more accurate dust mineralogy data, particularly from satellite observations, can have a significant impact on the amount of solar radiation reflected back to space, thereby influencing the radiative balance at the TOA. The transition from negative to positive forcing at the TOA emphasizes the importance of incorporating realistic mineralogical information to enhance the accuracy of dust-related radiative forcing calculations and better understand their role in climate systems.

### 3.3 Radiative effect on air quality

Aerosol effects not only gave rise to changes in meteorological variables but also had a significant impact on air quality. As shown in Fig. 7 and Table S3, the inclusion of bulk dust aerosol feedbacks in the WRF-CHIMERE model resulted in substantial increases in  $\text{PM}_{10}$  concentrations, with an average increase of  $119.48 \mu\text{g m}^{-3}$  with a 95 % CI of  $-27.63$  to  $1408.39 \mu\text{g m}^{-3}$ . This rise in particulate matter highlights the important role of dust aerosols in contributing to local and regional air pollution, especially in regions that are susceptible to dust storms. Along with these increases in  $\text{PM}_{10}$  concentrations,  $\text{O}_3$  concentrations slightly decreased, with an average reduction of  $-46.52 \mu\text{g m}^{-3}$ . This reduction in ozone can be attributed to the complex interaction between dust particles and ozone precursor gases, where dust aerosols can act as both a sink for ozone and influence the photochemical processes that govern its formation and degradation. These reactions would be related to the adsorption and catalytic decomposition of ozone on the surface of mineral dust particles, as well as the potential for dust to alter the concentration of reactive species in the atmosphere through heterogeneous chemistry (Cwiertny et al., 2008). For example, the presence of adsorbed water on dust particles can compete with ozone for reactive sites, reducing the overall uptake and decomposition of ozone (Usher et al., 2003). Additionally, the photochemical reactions involving dust particles, such as the photolysis of nitrate ions, can produce reactive radicals that further influence the atmospheric chemistry of ozone (Ma et al., 2021).

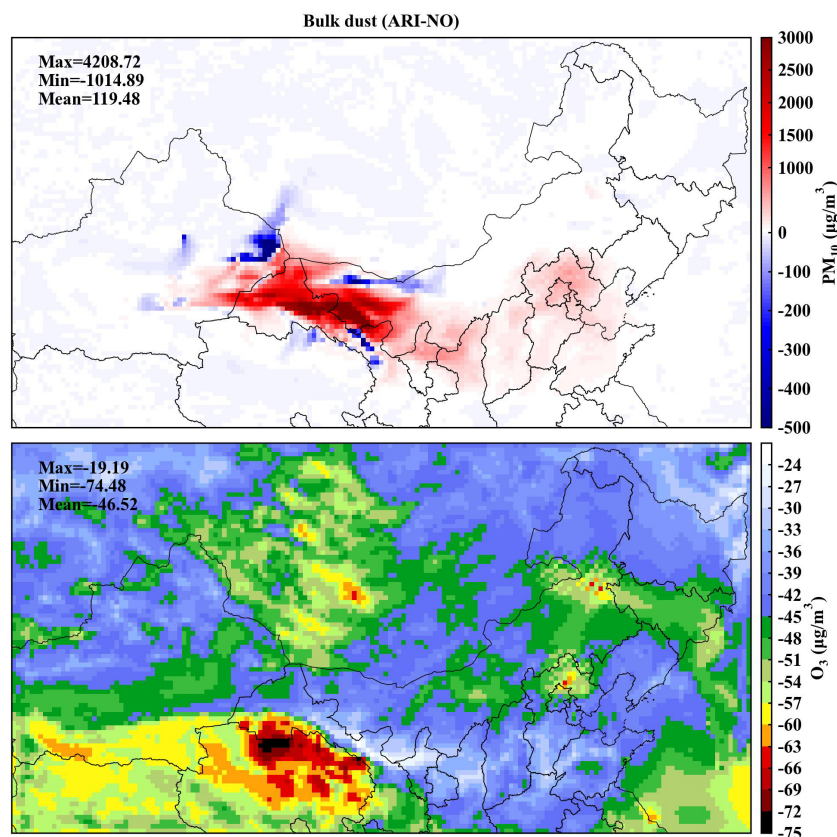


**Figure 7.** Changes in  $\text{PM}_{10}$  and  $\text{O}_3$  concentrations resulting from bulk dust-induced ARI effects, compared to the scenario without aerosol feedbacks.

The most pronounced increases in  $\text{PM}_{10}$  concentrations occurred in the Badain Jaran Desert, a well-known dust source region, where peak values exceeded  $1200 \mu\text{g m}^{-3}$ . This reflects the large dust emissions typical of desert environments, where strong winds mobilize vast quantities of particulate matter. Downwind regions, including Ningxia, Shaanxi, and Beijing, also experienced significant  $\text{PM}_{10}$  elevations, with concentration differences reaching approximately  $600 \mu\text{g m}^{-3}$  compared to baseline levels. The inclusion of speciated dust influences long-range transport and can substantially affect  $\text{PM}_{10}$  concentrations. Comparison of the subfigures in Fig. 8 reveals pronounced regional differences in  $\text{PM}_{10}$  predictions arising from the use of different mineralogical databases. Incorporating detailed mineralogical data enhances the accuracy of dust composition representation and its associated effects on  $\text{PM}_{10}$ , highlighting the critical role of mineral speciation in dust modeling and regional air quality assessment.

Ozone changes along transport pathways were generally smaller than the surrounding concentrations, typically ranging from  $-60$  to  $-40 \mu\text{g m}^{-3}$  with a mean value of  $-46.52 \mu\text{g m}^{-3}$  (95 % CI:  $-63.38$  to  $-31.74$ ) as shown in Table S3. These smaller changes in  $\text{O}_3$  concentrations reflect the fact that dust aerosols have a more localized and complex

effect on ozone formation and destruction, with significant variability depending on the regional and temporal context. In particular, dust-induced reductions in ozone are likely to be influenced by the local presence of other atmospheric constituents. The photochemical reactions involving dust particles, such as the photolysis of nitrate ions, can produce reactive radicals that further influence the atmospheric chemistry of ozone (Ma et al., 2021).

The spatial differences in  $\text{PM}_{10}$  and  $\text{O}_3$  concentrations simulated by WRF-CHIMERE with different mineralogy atlases compared to bulk dust, enabling ARI effects, are depicted in Figs. 8 and S4. These comparisons reveal substantial changes in the  $\text{PM}_{10}$  and  $\text{O}_3$  concentrations across the different mineralogical compositions, including N2012\_Default, N2012\_EMIT, J2014\_Default, J2014\_EMIT, and bulk dust. This suggests that the normalization of the 12 minerals from these atlases significantly modifies meteorological conditions, further influencing the relative abundances of dust particles and their subsequent effects on air quality and atmospheric composition.

When compared to bulk dust, reduced  $\text{PM}_{10}$  concentrations were primarily observed in the Taklimakan Desert, with decreases of around  $60 \mu\text{g m}^{-3}$ , while increases in  $\text{PM}_{10}$  concentrations occurred in the Badain Jaran Desert and its down-

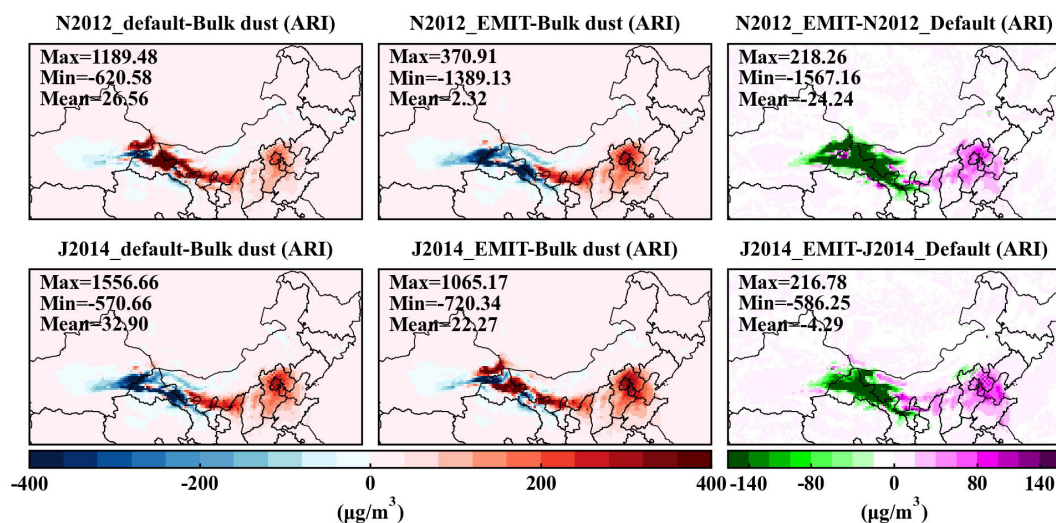


**Figure 8.** Difference in  $\text{PM}_{10}$  concentrations considering bulk dust and various dust mineralogy atlases that enable ARI effects.

wind regions, with concentrations rising up to  $1000 \mu\text{g m}^{-3}$ . These regional variations indicate that different dust mineralogical compositions can impact the emission and transport of dust, with certain mineral types leading to more efficient scattering or absorption of radiation, which may alter the local meteorological conditions and dust dispersion patterns.

For  $\text{O}_3$  concentrations, reductions and enhancements were mainly observed in the Horqin sandy land and North China Plain, with changes up to  $4 \mu\text{g m}^{-3}$ , respectively. This highlights the complex interaction between dust aerosols and ozone chemistry, where dust can either enhance or reduce ozone concentrations depending on the region. Dust aerosols can influence ozone levels by acting as a surface for heterogeneous chemical reactions or by modifying the photochemical processes that control ozone formation and destruction.

When considering the EMIT data,  $\text{PM}_{10}$  concentrations were reduced in dust source regions and enhanced in downwind regions, with reductions of up to  $-1567.16 \mu\text{g m}^{-3}$  and increases of  $+218.26 \mu\text{g m}^{-3}$ . This suggests that more accurate mineralogical data can influence dust transport patterns, leading to greater reductions in  $\text{PM}_{10}$  at the source regions and increased dust concentrations in the downwind areas. These findings further emphasize the role of mineralogical composition in modulating dust aerosol behavior and distribution.

For  $\text{O}_3$ , enhancements appeared in source regions, while reductions were observed in downwind regions, with changes ranging from  $-2.46$  to  $+3.52 \mu\text{g m}^{-3}$ . These trends suggest that more accurate dust speciation can influence regional ozone levels in different ways, with possible implications for local air quality and atmospheric chemistry. Notably, the impacts on  $\text{PM}_{10}$  concentrations from N2012\_EMIT compared to N2012\_Default were larger than those observed from J2014\_EMIT versus J2014\_Default, while the impacts on  $\text{O}_3$  concentrations followed the oppo-

site trends. This indicates that the choice of dust mineralogical dataset has a differential impact on  $\text{PM}_{10}$  and  $\text{O}_3$  concentrations, underscoring the importance of considering mineral composition in aerosol modeling to more accurately predict air quality and climate effects.

Figure 9 shows the percentage changes in surface concentrations of mineral dust with and without considering ARI effects. These results provide valuable insight into how the inclusion of ARI effects modifies the composition and radiative properties of dust aerosols, depending on the mineralogical dataset used. For the N2012\_Default and N2012\_EMIT data, quartz and feldspar accounted for a substantial portion of the total dust, ranging from approximately 51.7 % to 57.4 % for quartz and 18.6 % to 19.8 % for feldspar. This indicates that quartz and feldspar are the dominant mineral components in the dust modeled with the N2012 dataset.

In contrast, for the J2014\_Default dataset, the mineral composition was more diversified, with calcite, quartz, and mica contributing about 26.3 %, 24.0 %, and 20.0 %, respectively, to the total dust composition. This shift in mineral proportions reflects the differences in the mineralogical characterization between the N2012 and J2014 datasets, with J2014 incorporating a broader range of dust minerals. For J2014\_EMIT, the mineral composition shifted further, with quartz and mica making up approximately 46.8 % and 27.5 % of the dust, respectively. This highlights the importance of using accurate mineralogical data, such as that from EMIT satellite observations, to better represent the composition of dust aerosols in simulations.

The inclusion of EMIT data led to an increase in the absorption percentage of hematite by about 8 % for N2012 and 6 % for J2014. Hematite is a highly absorbing mineral, especially in the shortwave spectrum, and its increased presence enhances the dust's ability to absorb solar radiation, thereby affecting the DRE in the shortwave spectrum. This increase

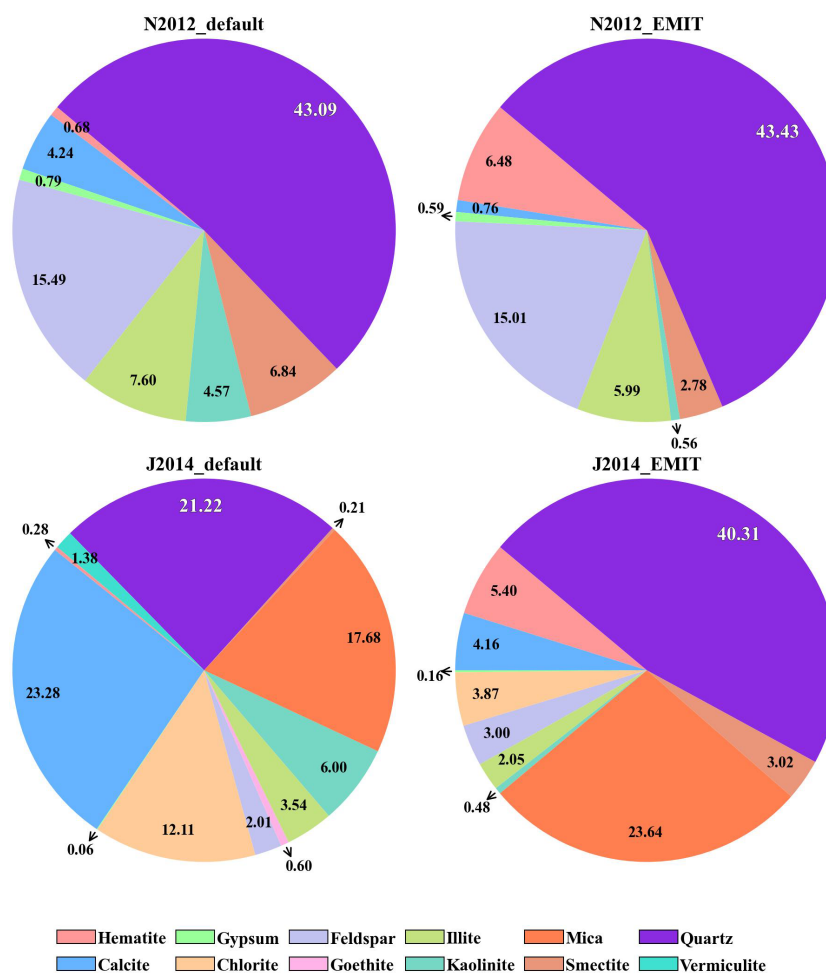


**Figure 9.** Contributions of different mineralogical compositions using N2012\_Default, N2012\_EMIT, J2014\_Default, and J2014\_EMIT, considering ARI effects, compared to the scenario without enabling aerosol feedbacks.

in hematite absorption is significant, as it directly impacts the radiative effects of dust, potentially contributing to a greater cooling effect on the atmosphere by modifying the shortwave radiation balance.

While quartz constitutes the largest portion of the dust in both the N2012 and J2014 datasets, its DRF effects are relatively limited, as noted in Li et al. (2021). Quartz is known for its high reflectivity in the shortwave spectrum, and while it makes up a large fraction of the total dust mass, it has a less pronounced effect on radiative forcing compared to more absorbing minerals like hematite or mica. This suggests that, despite its dominance in dust composition, quartz plays a smaller role in modifying the energy balance of the atmosphere through direct radiative effects.

### 3.4 Limitations and uncertainties for aerosol feedbacks of mineralogical dust

The accuracy of simulated dust emission is intricately linked to soil properties, such as soil texture and moisture, which

primarily influence the threshold friction velocity required for dust particle mobilization (Kim and Choi, 2015; Su and Fung, 2015). These factors play a critical role in determining the magnitude and spatial distribution of dust emissions, underscoring the need for precise and high-resolution soil data in dust modeling. While the current EMIT L3 data offers a spatial resolution of  $0.5^\circ \times 0.5^\circ$ , real-time higher spatial resolution datasets, such as the  $60\text{ m} \times 60\text{ m}$  EMIT L2B mineral atlas ([https://earth.jpl.nasa.gov/emit/internal\\_resources/282](https://earth.jpl.nasa.gov/emit/internal_resources/282), last access: 14 March 2026), can provide a more detailed representation of soil mineralogy, thereby enhancing the fidelity of dust emission simulations.

The uncertainty associated with dust mineralogical datasets is being actively addressed by NASA's EMIT. This initiative has deployed a hyperspectral imaging spectrometer aboard the International Space Station to deliver global retrievals of soil mineral compositions with unprecedented spatial detail. The spectrometer captures spectral absorption features within the UV to near-infrared range ( $0.38\text{--}2.5\ \mu\text{m}$ ), offering critical insights into the distribution and variability of

soil minerals (Castellanos et al., 2024; Connelly et al., 2021). In addition to satellite-based observations, ground-based stations play a vital role in measuring dust mineralogical compositions using stationary instruments, which provide localized and highly accurate data. Complementing these measurements, aircraft-based instruments offer the capability to sample dust particles along specific flight tracks, providing valuable vertical and spatial profiles of speciated dust properties (e.g., size and mixing state, Panta et al., 2023; Ryder et al., 2015). Together, these observational platforms form a robust foundation for validating and improving dust models.

Aerosol–cloud interactions involving speciated dust are another critical aspect of dust–climate interactions that require further investigation, especially for feldspar and quartz (Atkinson et al., 2013; Chatziparaschos et al., 2023). Incorporating these interactions into two-way coupled WRF–CHIMERE models can provide a more comprehensive understanding of the feedback mechanisms between dust aerosols and cloud microphysics. Such implementations are currently a focus of ongoing work, aiming to refine the representation of dust-induced radiative and microphysical effects in regional and global models. These efforts will not only improve model accuracy but also enhance our ability to predict the impacts of dust on weather, air quality, and climate.

## 4 Conclusion

Dust mineral composition plays a vital role in regulating atmospheric radiation and air quality, yet its effects remain poorly constrained in current atmospheric models. Understanding these impacts is particularly important for North China, where severe dust storms frequently affect regional climate and pollution. This study investigates how variations in mineral composition influence aerosol–radiation interactions and their implications for meteorology and air quality during a major dust storm event.

The findings revealed significant spatial variations in radiative forcing due to differences in dust mineralogy. Compared to the ARI effects of bulk dust, the mineralogical composition of dust aerosols can increase SW radiation forcing at the surface and in the atmosphere by  $+0.10$  to  $+0.82 \text{ W m}^{-2}$ , while simultaneously causing a decrease of approximately  $-0.72 \text{ W m}^{-2}$  in SW radiation forcing at the TOA. Integrating EMIT data into the model reduced  $\text{PM}_{10}$  biases by over 15 % in high-concentration regions and improved ozone predictions, with localized changes ranging from  $-2.46$  to  $+3.52 \mu\text{g m}^{-3}$ . Specifically, the ARI effects of these mineralogical compositions led to a notable increase in  $\text{PM}_{10}$  levels, reaching up to  $1189.48 \mu\text{g m}^{-3}$  in dust source regions, when compared to bulk dust scenarios.

These findings highlight the importance of incorporating dust mineralogical data to improve simulations of radiative forcing and air quality impacts. Within the scope of this study, the results indicate that overall dust mineralog-

ical composition, rather than dust mass alone, plays a decisive role in ARI effects, with hematite exerting a dominant influence despite its minor abundance, although the radiative effects of individual mineral species were not separately quantified. Systematic biases in surface radiation, near-surface winds, and temperature persist, reflecting challenges in simulating dust–atmosphere interactions and uncertainties in mineralogical datasets. Incorporating meteorological spectral nudging in future simulations could provide a more realistic representation of ARI-induced dust perturbations under different mineralogical compositions. Coupling this approach with higher-resolution soil and satellite data, as well as additional observational constraints, would further refine dust emission simulations and reduce model biases, particularly in regions frequently affected by severe dust events.

**Code and data availability.** The meteorological ICs and BCs, Chemical ICs and BCs and emission data used for WRF–CHIMERE and all data used to create figures and tables in this study are provided in an open repository on Zenodo (<https://doi.org/10.5281/zenodo.14728874>, Gao et al., 2025a). Himawari and CALIPSO satellite data are available at <ftp://ftp.ptree.jaxa.jp/jma/netcdf> (last access: 14 March 2026) and <https://subset.larc.nasa.gov/calipso> (last access: 14 March 2026), respectively.

The source codes of the two-way coupled WRFv3.7.1–CHIMERE v2020r3 models are obtained from <https://www.lmd.polytechnique.fr/chimere> (last access: 14 March 2026). The related source codes, configuration information, namelist files and automated run scripts of these three two-way coupled models are archived at Zenodo with the following associated DOI: <https://doi.org/10.5281/zenodo.14729124> (Gao et al., 2025b).

**Supplement.** The supplement related to this article is available online at <https://doi.org/10.5194/acp-26-3765-2026-supplement>.

**Author contributions.** CG, XZ, HY and LH carried out the data collection, related analysis, figure plotting, and paper writing. HZ, SZ, and AX were involved with the original research plan and made suggestions for the paper writing.

**Competing interests.** The contact author has declared that none of the authors has any competing interests.

**Disclaimer.** Publisher's note: Copernicus Publications remains neutral with regard to jurisdictional claims made in the text, published maps, institutional affiliations, or any other geographical representation in this paper. The authors bear the ultimate responsibility for providing appropriate place names. Views expressed in the text are those of the authors and do not necessarily reflect the views of the publisher.

**Acknowledgements.** This study was financially sponsored by the National Natural Science Foundation of China (grant nos. 42305171, 42371154 and 42171142), the Natural Science Foundation of Jilin Province (YDZJ202201ZYTS476), the National Key Scientific and Technological Infrastructure project “Earth System Numerical Simulation Facility” (2023-EL-PT-000469), the Youth Innovation Promotion Association of Chinese Academy of Sciences, China (grant nos. 2022230), the National Key Research and Development Program of China (grant nos. 2017YFC0212304 and 2019YFE0194500) and the Talent Program of Chinese Academy of Sciences (Y8H1021001).

**Financial support.** This research has been supported by the National Natural Science Foundation of China (grant nos. 42305171, 42371154, and 42171142).

**Review statement.** This paper was edited by N’Datchoh Evelyne Touré and reviewed by two anonymous referees.

## References

- Adebisi, A., Kok, J. F., Murray, B. J., Ryder, C. L., Stuu, J.-B. W., Kahn, R. A., Knippertz, P., Formenti, P., Mahowald, N. M., and García-Pando, C. P.: A review of coarse mineral dust in the Earth system, *Aeolian Res.*, 60, 100849, <https://doi.org/10.1016/j.aeolia.2022.100849>, 2023.
- Alapaty, K., Herwehe, J. A., Otte, T. L., Nolte, C. G., Bullock, O. R., Mallard, M. S., Kain, J. S., and Dudhia, J.: Introducing subgrid-scale cloud feedbacks to radiation for regional meteorological and climate modeling, *Geophys. Res. Lett.*, 39, <https://doi.org/10.1029/2012GL054031>, 2012.
- Alfaro, S., Lafon, S., Rajot, J., Formenti, P., Gaudichet, A., and Maille, M.: Iron oxides and light absorption by pure desert dust: An experimental study, *J. Geophys. Res.-Atmos.*, 109, <https://doi.org/10.1029/2003JD004374>, 2004.
- Atkinson, J. D., Murray, B. J., Woodhouse, M. T., Whale, T. F., Baustian, K. J., Carslaw, K. S., Dobbie, S., O’Sullivan, D., and Malkin, T. L.: The importance of feldspar for ice nucleation by mineral dust in mixed-phase clouds, *Nature*, 498, 355–358, <https://doi.org/10.1038/nature12278>, 2013.
- Balkanski, Y., Bonnet, R., Boucher, O., Checa-Garcia, R., and Servonnat, J.: Better representation of dust can improve climate models with too weak an African monsoon, *Atmos. Chem. Phys.*, 21, 11423–11435, <https://doi.org/10.5194/acp-21-11423-2021>, 2021.
- Briant, R., Tuccella, P., Deroubaix, A., Khvorostyanov, D., Menut, L., Mailler, S., and Turquety, S.: Aerosol–radiation interaction modelling using online coupling between the WRF 3.7.1 meteorological model and the CHIMERE 2016 chemistry-transport model, through the OASIS3-MCT coupler, *Geosci. Model Dev.*, 10, 927–944, <https://doi.org/10.5194/gmd-10-927-2017>, 2017.
- Castellanos, P., Colarco, P., Espinosa, W. R., Guzewich, S. D., Levy, R. C., Miller, R. L., Chin, M., Kahn, R. A., Kemppinen, O., and Moosmüller, H.: Mineral dust optical properties for remote sensing and global modeling: A review, *Remote Sens. Environ.*, 303, 113982, <https://doi.org/10.1016/j.rse.2023.113982>, 2024.
- Chatziparaschos, M., Daskalakis, N., Myriokefalitakis, S., Kalivitis, N., Nenes, A., Gonçalves Ageitos, M., Costa-Surós, M., Pérez García-Pando, C., Zanolli, M., Vrekoussis, M., and Kanakidou, M.: Role of K-feldspar and quartz in global ice nucleation by mineral dust in mixed-phase clouds, *Atmos. Chem. Phys.*, 23, 1785–1801, <https://doi.org/10.5194/acp-23-1785-2023>, 2023.
- Choobari, O. A., Zawar-Reza, P., and Sturman, A.: The global distribution of mineral dust and its impacts on the climate system: A review, *Atmos. Res.*, 138, 152–165, <https://doi.org/10.1016/j.atmosres.2013.11.007>, 2014.
- Claquin, T., Schulz, M., and Balkanski, Y.: Modeling the mineralogy of atmospheric dust sources, *J. Geophys. Res.-Atmos.*, 104, 22243–22256, <https://doi.org/10.1029/1999JD900416>, 1999.
- Connelly, D. S., Thompson, D. R., Mahowald, N. M., Li, L., Carmon, N., Okin, G. S., and Green, R. O.: The EMIT mission information yield for mineral dust radiative forcing, *Remote Sens. Environ.*, 258, 112380, <https://doi.org/10.1016/j.rse.2021.112380>, 2021.
- Cwiertny, D. M., Young, M. A., and Grassian, V. H.: Chemistry and photochemistry of mineral dust aerosol, *Annu. Rev. Phys. Chem.*, 59, 27–51, <https://doi.org/10.1146/annurev.physchem.59.032607.093630>, 2008.
- Duniway, M. C., Pfennigwerth, A. A., Fick, S. E., Nauman, T. W., Belnap, J., and Barger, N. N.: Wind erosion and dust from US drylands: a review of causes, consequences, and solutions in a changing world, *Ecosphere*, 10, e02650, <https://doi.org/10.1002/ecs2.2650>, 2019.
- Fécan, F., Marticorena, B., and Bergametti, G.: Parametrization of the increase of the aeolian erosion threshold wind friction velocity due to soil moisture for arid and semi-arid areas, *Ann. Geophys.*, 17, 149–157, <https://doi.org/10.1007/s00585-999-0149-7>, 1998.
- Formenti, P., Caquineau, S., Desboeufs, K., Klaver, A., Chevillier, S., Journet, E., and Rajot, J. L.: Mapping the physico-chemical properties of mineral dust in western Africa: mineralogical composition, *Atmos. Chem. Phys.*, 14, 10663–10686, <https://doi.org/10.5194/acp-14-10663-2014>, 2014.
- Gao, C., Xiu, A., Zhang, X., Tong, Q., Zhao, H., Zhang, S., Yang, G., and Zhang, M.: Two-way coupled meteorology and air quality models in Asia: a systematic review and meta-analysis of impacts of aerosol feedbacks on meteorology and air quality, *Atmos. Chem. Phys.*, 22, 5265–5329, <https://doi.org/10.5194/acp-22-5265-2022>, 2022.
- Gao, C., Zhang, X., Xiu, A., Tong, Q., Zhao, H., Zhang, S., Yang, G., Zhang, M., and Xie, S.: Intercomparison of multiple two-way coupled meteorology and air quality models (WRF v4.1.1–CMAQ v5.3.1, WRF–Chem v4.1.1, and WRF v3.7.1–CHIMERE v2020r1) in eastern China, *Geosci. Model Dev.*, 17, 2471–2492, <https://doi.org/10.5194/gmd-17-2471-2024>, 2024.
- Gao, C., Zhang, X., Yang, H., Huang, L., Zhao, H., Zhang, S., and Xiu, A.: The role of dust mineral composition in atmospheric radiation and pollution in North China: new insights from EMIT and two-way coupled modeling for JGR–Atmosphere paper (0.0.1), Zenodo [data set], <https://doi.org/10.5281/zenodo.14728874>, 2025a.
- Gao, C., Zhang, X., Yang, H., Huang, L., Zhao, H., Zhang, S., and Xiu, A.: The role of dust mineral composition in atmospheric radiation and pollution in North China:

- new insights from EMIT and two-way coupled modeling for JGR-atmosphere paper (0.0.1), Zenodo [code], <https://doi.org/10.5281/zenodo.14729124>, 2025b.
- Gómez Maqueo Anaya, S., Althausen, D., Faust, M., Baars, H., Heinold, B., Hofer, J., Tegen, I., Ansmann, A., Engelmann, R., Skupin, A., Heese, B., and Schepanski, K.: The implementation of dust mineralogy in COSMO5.05-MUSCAT, *Geosci. Model Dev.*, 17, 1271–1295, <https://doi.org/10.5194/gmd-17-1271-2024>, 2024.
- Gonçalves Ageitos, M., Obiso, V., Miller, R. L., Jorba, O., Klose, M., Dawson, M., Balkanski, Y., Perlwitz, J., Basart, S., Di Tomaso, E., Escribano, J., Macchia, F., Montané, G., Mahowald, N. M., Green, R. O., Thompson, D. R., and Pérez García-Pando, C.: Modeling dust mineralogical composition: sensitivity to soil mineralogy atlases and their expected climate impacts, *Atmos. Chem. Phys.*, 23, 8623–8657, <https://doi.org/10.5194/acp-23-8623-2023>, 2023.
- Green, R. O., Mahowald, N., Ung, C., Thompson, D. R., Bator, L., Bennet, M., Bernas, M., Blackway, N., Bradley, C., and Cha, J.: The Earth surface mineral dust source investigation: An Earth science imaging spectroscopy mission, 2020 IEEE aerospace conference, 1–15, <https://doi.org/10.1109/AERO47225.2020.9172731>, 2020.
- Harrison, A. D., Whale, T. F., Carpenter, M. A., Holden, M. A., Neve, L., O'Sullivan, D., Vergara Temprado, J., and Murray, B. J.: Not all feldspars are equal: a survey of ice nucleating properties across the feldspar group of minerals, *Atmos. Chem. Phys.*, 16, 10927–10940, <https://doi.org/10.5194/acp-16-10927-2016>, 2016.
- Journet, E., Balkanski, Y., and Harrison, S. P.: A new data set of soil mineralogy for dust-cycle modeling, *Atmos. Chem. Phys.*, 14, 3801–3816, <https://doi.org/10.5194/acp-14-3801-2014>, 2014.
- Ke, Z., Liu, X., Wu, M., Shan, Y., and Shi, Y.: Improved dust representation and impacts on dust transport and radiative effect in CAM5, *J. Adv. Model. Earth Sy.*, 14, e2021MS002845, <https://doi.org/10.1029/2021MS002845>, 2022.
- Kim, H. and Choi, M.: Impact of soil moisture on dust outbreaks in East Asia: Using satellite and assimilation data, *Geophys. Res. Lett.*, 42, 2789–2796, <https://doi.org/10.1002/2015GL063325>, 2015.
- Klingmüller, K., Lelieveld, J., Karydis, V. A., and Stenchikov, G. L.: Direct radiative effect of dust–pollution interactions, *Atmos. Chem. Phys.*, 19, 7397–7408, <https://doi.org/10.5194/acp-19-7397-2019>, 2019.
- Kok, J. F., Mahowald, N. M., Fratini, G., Gillies, J. A., Ishizuka, M., Leys, J. F., Mikami, M., Park, M.-S., Park, S.-U., Van Pelt, R. S., and Zobeck, T. M.: An improved dust emission model – Part 1: Model description and comparison against measurements, *Atmos. Chem. Phys.*, 14, 13023–13041, <https://doi.org/10.5194/acp-14-13023-2014>, 2014.
- Kok, J. F., Ridley, D. A., Zhou, Q., Miller, R. L., Zhao, C., Heald, C. L., Ward, D. S., Albani, S., and Haustein, K.: Smaller desert dust cooling effect estimated from analysis of dust size and abundance, *Nat. Geosci.*, 10, 274–278, <https://doi.org/10.1038/ngeo2912>, 2017.
- Kok, J. F., Storelvmo, T., Karydis, V. A., Adebisi, A. A., Mahowald, N. M., Evan, A. T., He, C., and Leung, D. M.: Mineral dust aerosol impacts on global climate and climate change, *Nature Reviews Earth & Environment*, 4, 71–86, <https://doi.org/10.1038/s43017-022-00379-5>, 2023.
- Kumar, A., Marcolli, C., Luo, B., and Peter, T.: Ice nucleation activity of silicates and aluminosilicates in pure water and aqueous solutions – Part 1: The K-feldspar microcline, *Atmos. Chem. Phys.*, 18, 7057–7079, <https://doi.org/10.5194/acp-18-7057-2018>, 2018.
- Lafon, S., Sokolik, I. N., Rajot, J. L., Caquineau, S., and Gaudichet, A.: Characterization of iron oxides in mineral dust aerosols: Implications for light absorption, *J. Geophys. Res.-Atmos.*, 111, <https://doi.org/10.1029/2005JD007016>, 2006.
- Li, L. and Sokolik, I. N.: The dust direct radiative impact and its sensitivity to the land surface state and key minerals in the WRF-Chem-DuMo Model: a case study of dust storms in Central Asia, *J. Geophys. Res.-Atmos.*, 123, 4564–4582, <https://doi.org/10.1029/2017JD027667>, 2018.
- Li, L., Mahowald, N. M., Miller, R. L., Pérez García-Pando, C., Klose, M., Hamilton, D. S., Gonçalves Ageitos, M., Ginoux, P., Balkanski, Y., Green, R. O., Kalashnikova, O., Kok, J. F., Obiso, V., Paynter, D., and Thompson, D. R.: Quantifying the range of the dust direct radiative effect due to source mineralogy uncertainty, *Atmos. Chem. Phys.*, 21, 3973–4005, <https://doi.org/10.5194/acp-21-3973-2021>, 2021.
- Li, L., Mahowald, N. M., Kok, J. F., Liu, X., Wu, M., Leung, D. M., Hamilton, D. S., Emmons, L. K., Huang, Y., Sexton, N., Meng, J., and Wan, J.: Importance of different parameterization changes for the updated dust cycle modeling in the Community Atmosphere Model (version 6.1), *Geosci. Model Dev.*, 15, 8181–8219, <https://doi.org/10.5194/gmd-15-8181-2022>, 2022.
- Li, L., Mahowald, N. M., Gonçalves Ageitos, M., Obiso, V., Miller, R. L., Pérez García-Pando, C., Di Biagio, C., Formenti, P., Brodrick, P. G., and Clark, R. N.: Improved constraints on hematite refractive index for estimating climatic effects of dust aerosols, *Communications Earth & Environment*, 5, 295, <https://doi.org/10.1038/s43247-024-01441-4>, 2024.
- Ma, Q., Zhong, C., Ma, J., Ye, C., Zhao, Y., Liu, Y., Zhang, P., Chen, T., Liu, C., and Chu, B.: Comprehensive study about the photolysis of nitrates on mineral oxides, *Environ. Sci. Technol.*, 55, 8604–8612, <https://doi.org/10.1021/acs.est.1c02182>, 2021.
- Maher, B. A., Prospero, J. M., Mackie, D., Gaiero, D., Hesse, P. P., and Balkanski, Y.: Global connections between aeolian dust, climate and ocean biogeochemistry at the present day and at the last glacial maximum, *Earth-Sci. Rev.*, 99, 61–97, <https://doi.org/10.1016/j.earscirev.2009.12.001>, 2010.
- Menut, L., Siour, G., Bessagnet, B., Couvidat, F., Journet, E., Balkanski, Y., and Desboeufs, K.: Modelling the mineralogical composition and solubility of mineral dust in the Mediterranean area with CHIMERE 2017r4, *Geosci. Model Dev.*, 13, 2051–2071, <https://doi.org/10.5194/gmd-13-2051-2020>, 2020.
- Menut, L., Bessagnet, B., Cholakian, A., Siour, G., Mailler, S., and Pennel, R.: What is the relative impact of nudging and online coupling on meteorological variables, pollutant concentrations and aerosol optical properties?, *Geosci. Model Dev.*, 17, 3645–3665, <https://doi.org/10.5194/gmd-17-3645-2024>, 2024.
- Nickovic, S., Vukovic, A., Vujadinovic, M., Djurdjevic, V., and Pejanovic, G.: Technical Note: High-resolution mineralogical database of dust-productive soils for atmospheric dust modeling, *Atmos. Chem. Phys.*, 12, 845–855, <https://doi.org/10.5194/acp-12-845-2012>, 2012.

- Obiso, V., Gonçalves Ageitos, M., Pérez García-Pando, C., Perlwitz, J. P., Schuster, G. L., Bauer, S. E., Di Biagio, C., Formenti, P., Tsigaridis, K., and Miller, R. L.: Observationally constrained regional variations of shortwave absorption by iron oxides emphasize the cooling effect of dust, *Atmos. Chem. Phys.*, 24, 5337–5367, <https://doi.org/10.5194/acp-24-5337-2024>, 2024.
- Pang, M., Jin, J., Segers, A., Jiang, H., Han, W., Buyantogtokh, B., Xia, J., Fang, L., Li, J., Lin, H. X., and Liao, H.: Valid time shifting ensemble Kalman filter (VTS-EnKF) for dust storm forecasting, *Geosci. Model Dev.*, 17, 8223–8242, <https://doi.org/10.5194/gmd-17-8223-2024>, 2024.
- Panta, A., Kandler, K., Alastuey, A., González-Flórez, C., González-Romero, A., Klose, M., Querol, X., Reche, C., Yus-Díez, J., and Pérez García-Pando, C.: Insights into the single-particle composition, size, mixing state, and aspect ratio of freshly emitted mineral dust from field measurements in the Moroccan Sahara using electron microscopy, *Atmos. Chem. Phys.*, 23, 3861–3885, <https://doi.org/10.5194/acp-23-3861-2023>, 2023.
- Ryder, C. L., McQuaid, J. B., Flamant, C., Rosenberg, P. D., Washington, R., Brindley, H. E., Highwood, E. J., Marsham, J. H., Parker, D. J., Todd, M. C., Banks, J. R., Brooke, J. K., Engelstaedter, S., Estelles, V., Formenti, P., Garcia-Carreras, L., Kocha, C., Marengo, F., Sodemann, H., Allen, C. J. T., Bourdon, A., Bart, M., Cavazos-Guerra, C., Chevaillier, S., Crosier, J., Darbyshire, E., Dean, A. R., Dorsey, J. R., Kent, J., O’Sullivan, D., Schepanski, K., Szpek, K., Trembath, J., and Woolley, A.: Advances in understanding mineral dust and boundary layer processes over the Sahara from Fennec aircraft observations, *Atmos. Chem. Phys.*, 15, 8479–8520, <https://doi.org/10.5194/acp-15-8479-2015>, 2015.
- Scanza, R. A., Mahowald, N., Ghan, S., Zender, C. S., Kok, J. F., Liu, X., Zhang, Y., and Albani, S.: Modeling dust as component minerals in the Community Atmosphere Model: development of framework and impact on radiative forcing, *Atmos. Chem. Phys.*, 15, 537–561, <https://doi.org/10.5194/acp-15-537-2015>, 2015.
- Schepanski, K.: Transport of mineral dust and its impact on climate, *Geosciences*, 8, 151, <https://doi.org/10.3390/geosciences8050151>, 2018.
- Shao, Y. and Lu, H.: A simple expression for wind erosion threshold friction velocity, *J. Geophys. Res.-Atmos.*, 105, 22437–22443, <https://doi.org/10.1029/2000JD900304>, 2000.
- Shao, Y., Wyrwoll, K.-H., Chappell, A., Huang, J., Lin, Z., McTainsh, G. H., Mikami, M., Tanaka, T. Y., Wang, X., and Yoon, S.: Dust cycle: An emerging core theme in Earth system science, *Aeolian Res.*, 2, 181–204, <https://doi.org/10.1016/j.aeolia.2011.02.001>, 2011.
- Sokolik, I. N. and Toon, O. B.: Incorporation of mineralogical composition into models of the radiative properties of mineral aerosol from UV to IR wavelengths, *J. Geophys. Res.*, 104, 9423–9444, <https://doi.org/10.1029/1998JD200048>, 1999.
- Solomos, S., Spyrou, C., Bartsotas, N. S., Sykioti, O., Amiridis, V., Gkikas, A., Marinou, E., Katsafados, P., Tsarpalis, K., and Pejanovic, G.: The Development of a Dust Mineralogy Map from Satellite Retrievals and Implementation in WRF-Chem, *Environmental Sciences Proceedings*, 26, 54, <https://doi.org/10.3390/envirosci2023026054>, 2023a.
- Solomos, S., Spyrou, C., Barreto, A., Rodríguez, S., González, Y., Neophytou, M. K., Mouzourides, P., Bartsotas, N. S., Kalogerí, C., and Nickovic, S.: The development of METAL-WRF Regional Model for the Description of Dust Mineralogy in the Atmosphere, *Atmosphere-Basel*, 14, 1615, <https://doi.org/10.3390/atmos14111615>, 2023b.
- Song, Q., Ginoux, P., Gonçalves Ageitos, M., Miller, R. L., Obiso, V., and Pérez García-Pando, C.: Modeling impacts of dust mineralogy on fast climate response, *Atmos. Chem. Phys.*, 24, 7421–7446, <https://doi.org/10.5194/acp-24-7421-2024>, 2024.
- Su, L. and Fung, J. C.: Sensitivities of WRF-Chem to dust emission schemes and land surface properties in simulating dust cycles during springtime over East Asia, *J. Geophys. Res.-Atmos.*, 120, 11–215, <https://doi.org/10.1002/2015JD023446>, 2015.
- Tang, W., Yang, K., Qin, J., Li, X., and Niu, X.: A 16 year dataset (2000–2015) of high-resolution (3 h, 10 km) global surface solar radiation, *Earth Syst. Sci. Data*, 11, 1905–1915, <https://doi.org/10.5194/essd-11-1905-2019>, 2019.
- Tong, D. Q., Gill, T. E., Sprigg, W. A., Van Pelt, R. S., Baklanov, A. A., Barker, B. M., Bell, J. E., Castillo, J., Gassó, S., and Gaston, C. J.: Health and safety effects of airborne soil dust in the Americas and beyond, *Rev. Geophys.*, 61, e2021RG000763, <https://doi.org/10.1029/2021RG000763>, 2023.
- Tuccella, P., Menut, L., Briant, R., Deroubaix, A., Khvorostyanov, D., Mailler, S., Siour, G., and Turquety, S.: Implementation of Aerosol-Cloud Interaction within WRF-CHIMERE Online Coupled Model: Evaluation and Investigation of the Indirect Radiative Effect from Anthropogenic Emission Reduction on the Benelux Union, *Atmosphere-Basel*, 10, 20, <https://doi.org/10.3390/atmos10010020>, 2019.
- Usher, C. R., Michel, A. E., and Grassian, V. H.: Reactions on mineral dust, *Chem. Rev.*, 103, 4883–4940, <https://doi.org/10.1021/cr020657y>, 2003.
- Wang, X., Zhang, L., and Moran, M. D.: Development of a new semi-empirical parameterization for below-cloud scavenging of size-resolved aerosol particles by both rain and snow, *Geosci. Model Dev.*, 7, 799–819, <https://doi.org/10.5194/gmd-7-799-2014>, 2014.
- Willis, P. T. and Tattelman, P.: Drop-size distributions associated with intense rainfall, *J. Appl. Meteorol. Clim.*, 28, 3–15, [https://doi.org/10.1175/1520-0450\(1989\)028<0003:DSDAWI>2.0.CO;2](https://doi.org/10.1175/1520-0450(1989)028<0003:DSDAWI>2.0.CO;2), 1989.
- Zhang, L., Gong, S., Padro, J., and Barrie, L.: A size-segregated particle dry deposition scheme for an atmospheric aerosol module, *Atmos. Environ.*, 35, 549–560, [https://doi.org/10.1016/S1352-2310\(00\)00326-5](https://doi.org/10.1016/S1352-2310(00)00326-5), 2001.
- Zuo, X., Zhang, C., Zhang, X., Wang, R., Zhao, J., and Li, W.: Wind tunnel simulation of wind erosion and dust emission processes, and the influences of soil texture, *International Soil and Water Conservation Research*, 12, 455–466, <https://doi.org/10.1016/j.iswcr.2023.08.005>, 2024.